

Refraction angle extracting strategy for fan-beam differential phase contrast CT

Renzhen Ye^a, Yi Tang^b, Xiaoqiang Lu^{c,*}

^a College of Sciences, Huazhong Agricultural University, Wuhan 430074, Hubei, PR China

^b School of Mathematics and Computer Science, Yunnan University of Nationalities, Kunming, 650500 Yunnan, PR China

^c The Center for OPTical IMagery Analysis and Learning (OPTIMAL), State Key Laboratory of Transient Optics and Photonics, Xi'an Institute of Optics and Precision Mechanics, Chinese Academy of Sciences, Xi'an 710119, Shaanxi, PR China

ARTICLE INFO

Article history:

Received 12 October 2013

Received in revised form

22 March 2014

Accepted 23 March 2014

Communicated by X. Gao

Available online 13 April 2014

Keywords:

Phase-contrast image

X-ray imaging

Fan-beam CT

PI-line

Gratings interferometer

ABSTRACT

In this paper, the fan-beam *differential phase contrast computed tomography* (DPC-CT) reconstruction method is studied. We first present a new vision of how to implement the *Reverse-Projection* (RP) method to extract the refraction-angle data efficiently in fan-beam geometry, and then provide a Katsevich-type formula for fan-beam DPC-CT reconstruction. The proposed method has two key properties. First, it is essentially a *filtered back projection* (FBP) reconstruction formula. Second, it can deal with incomplete data sets. The main contributions of this paper lie in the following three aspects: First, the physical principle of the bent-grating based fan-beam DPC imaging is discussed and the RP-method is extended to the fan-beam case. Second, an implementation strategy of Katsevich algorithm for fan-beam DPC-CT is proposed. Third, a semi-quantitative research on the influence of the approximation errors introduced by the RP-method is carried out by using several numerical simulations. It should be pointed out that the RP-method will certainly introduce some errors. The effect of these errors on our reconstruction algorithm is discussed by several numerical simulations.

© 2014 Elsevier B.V. All rights reserved.

1. Introduction

Phase-contrast (PC) imaging is a novel X-ray inspection method which uses the refraction rather than the absorption as the imaging signal and offers more internal structure details [4]. Until now, several X-ray PC imaging methods have been proposed and they can be divided into four categories: interferometer based methods [5–7], propagation based methods [8–10], analyzer based methods [11–13] and grating [14–20] based methods, which are differentiated from one another by measuring either the zero-order, the first-order or the second-order derivatives of the phase distribution. These three methods rely on the high coherence of synchrotron radiation sources or micro-focus tube [9,11], which is the main obstacle to clinical diagnosis of PC imaging.

In recent years, grating-based methods, which were initially implemented at X-ray synchrotron radiation sources [14,16], have been transferred to conventional X-ray tube sources [17–21]. In 2006, Pfeiffer et al., firstly, implemented PC imaging by using a conventional x-ray source [17,18]. In their methods, a source grating is adopted to create an array of line sources from the X-ray beams generated by a conventional X-ray source. Within

each line source, the X-rays are highly coherent. If the coherence length of each line source is much larger than the period of the phase grating, the self-imaging replica of the phase grating appears at the fractional Talbot distance and then the gradient of the phase distribution can be measured by a Talbot–Lau interferometer. In synchrotron radiation experiments, the radiation beams can be well approximated as parallel beams and the plane gratings are adopted. In conventional X-ray tube experiments, the source emits a fan/cone beam [1–3]. If the plane gratings are still used, only the small central part angle of the fan/cone beam near the optical axis of the imaging system can be effectively employed, which limits the application of PC imaging. To overcome this problem, Revol et al. used the cylindrical gratings instead of the plane gratings to realize the fan-beam differential phase-contrast imaging [14]. One major advantage of the aforementioned methods is to realize the compact X-ray *differential phase-contrast CT* (DPC-CT) system [18,22–29], which shows a great potential in medical diagnosis and industrial nondestructive test.

The aim of DPC-CT is to reconstruct the refractive index decrement from the refraction-angle data by using the X-ray scanner of a given geometry [41]. Generally, the refraction-angle data should be extracted by using the *phase-stepping* (PS) method [17,19]. This method assumes the sample to be stationary and requires several sampling attempts at each view angle, which leads to unacceptably long exposure time and huge X-ray doses.

* Corresponding author.

E-mail address: luxq66666@gmail.com (X. Lu).

In CT scanning, the sample is rotating round a fixed axis. The reverse projection (RP) [25] method has been proposed recently and extracted the refraction-angle data through rotation, which does not require phase stepping and is much simpler than the PS method. After the refraction-angle data was obtained, the DPC-CT algorithms [22–29] can be performed to reconstruct the refractive index distribution decrement. The reconstruction problem for parallel-beam DPC-CT is solved by the FBP algorithm [24,25] which has also been extended to fan/cone beam [26,27] scanning geometries. However, the FBP algorithm is known to be sensitive to incomplete data sets. Several algorithms have been developed to overcome the FBP's drawback. Two famous examples are BPF [30–33] and Katsevich-type [34–37] algorithms. The key difference between the two algorithms is the filtering-process. This difference leads to an interesting conclusion that in some cases the BPF algorithm is faster, whereas in another case the Katsevich algorithm is faster [33]. In 2008, the concept of BPF algorithm has been transferred to fan beam DPC-CT [28] by Chen and Qi, which shows great advantages over the conventional FBP algorithm. In 2011, Fu et al. provided a formulation of BPF algorithm for flat detector geometry [29]. However, they did not discuss the extraction of the refraction-angle under the fan-beam condition. In this paper, we first extend the RP method to the fan-beam condition and then discuss and analyze the implementation of the Katsevich algorithm for fan-beam DPC-CT. It should be pointed out that the RP-method will introduce some approximation errors. The influence of these errors on our reconstruction algorithm is analyzed by numerical simulations.

The rest of the paper is organized as follows. In Section 2, the physical theory of bent-grating interferometer is introduced and the RP method is extended to the fan-beam case. In Section 3, the 2D Katsevich's formula is briefly reviewed and the implementation of this formula for fan-beam DPC-CT reconstruction is proposed and analyzed. In Section 4, some numerical simulation results are given and discussed. The summary of our work is provided in Section 5.

2. The physical principle of fan-beam DPC-CT

The Talbot–Lau interferometer requires all the X-rays to be perpendicular to the gratings. In the fan-beam case, the X-ray beam is cylindrically divergent which illustrates that the cylindrical gratings are more suitable for fan-beam DPC-CT than the plane gratings [21].

2.1. Bent-grating interferometer formulas

We consider the cylindrical gratings based DPC imaging system shown in Fig. 1. In this system, the source grating G_0 , the phase grating G_1 and the absorption grating G_2 are distributed in three concentric circles with radius R_0 , R_1 and R_2 . If the X-ray source is placed at the center of concentric circles, the X-ray beams are perpendicular to the gratings at each direction.

The source grating G_0 shapes the cylindrical wave into an array of spatially coherent line sources. Each open of grating G_0 emits cylindrical waves which magnify the geometrical projection of G_1 onto G_2 . The geometrical magnification factor M is given by [38]

$$M = \frac{R_2 - R_0}{R_1 - R_0}. \quad (1)$$

The phase grating G_1 with the period p_1 introduces a phase shift on the incoming X-rays and produces the periodic fringes with the period p_2 at the Talbot distance. By considering the geometrical magnification factor M , the difference between the radius R_1 and R_2 should be rescaled according to the Fresnel

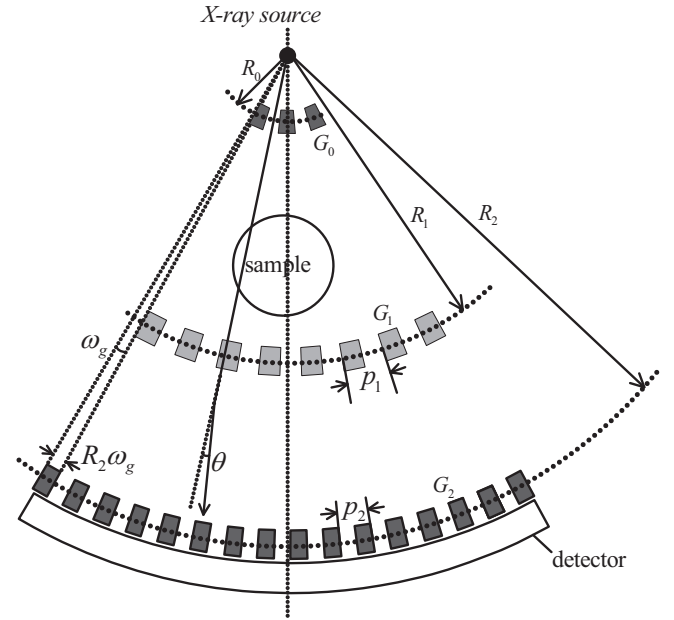


Fig. 1. Cylindrical gratings based DPC imaging system. Three cylindrical gratings G_0 , G_1 and G_2 are bent on three concentric circles with radius R_0 , R_1 and R_2 . The X-ray source is placed at the center of concentric circles.

scaling theorem [38]:

$$R_2 - R_1 = MD_T, \quad (2)$$

where D_T is the Fractional Talbot distance under parallel beam condition. By considering Eq. (2) for the radius R_2 , we find

$$R_2 = R_1 \frac{R_1 - R_0 - \frac{R_0}{R_1} D_T}{R_1 - R_0 - D_T}. \quad (3)$$

Based on the geometrical relationship $R_0 < R_1 < R_2$, we obtain that the prerequisite for the establishment of the Eq. (3) is

$$R_1 > R_0 + D_T. \quad (4)$$

By considering the geometrical magnification factor M , the period p_2 of the periodic fringes is given by

$$p_2 = M \frac{p_1}{\eta}, \quad (5)$$

where $\eta = 2$ for a π -phase modulation grating and $\eta = 1$ for a $\pi/2$ -phase modulation grating. The absorption grating G_2 with the same period as the fringes works as a gate to allow or prohibit most of the rays to be collected by the detector. When the pixel pitch of the detector is the integer times of or much larger than p_2 , the X-ray intensity on the detector depends on the relative shear displacement between the grating G_2 and the fringes. If a sample is placed either before or behind the phase grating G_1 , the refraction angle θ changes the location of the fringes and further changes the intensity on the detector. For weak scattering samples, the intensity I of each X-ray mainly includes the contribution of the absorption and refraction information [17–19,25]:

$$I = I_R \cdot S(\theta), \quad (6)$$

where I_R is the portion of the incident beam which has only been affected by absorption, θ is the refraction angle, and S is the shifting curve function. For small-value refraction angle, the shifting curve function can be expressed as a two-term Taylor series approximation at its half-slope:

$$S(\theta) = S_{\omega_g = p_2/4R_2} + \theta \cdot S'_{\omega_g = p_2/4R_2}, \quad (7)$$

where $S_{\omega_g} = p_2/4R_2$ and $S'_{\omega_g} = p_2/4R_2$ are the values of the shifting curve function S and its derivative at the half-slope, which requires that the angle ω_g equals to $p_2/4R_2$.

2.2. Refraction-angle retrieval in fan-beam case

Recently, the RP method was proposed to extract the refraction-angle under the parallel-beam condition [25], which significantly reduces the radiation dose. In this paper, we extend the RP-method to the fan-beam case. The scan model of the fan-beam DPC-CT is shown in Fig. 2. In the fixed coordinate system XOY , the X-ray source moves around the center along a circle trajectory. Each X-ray can be labeled by the source rotation angle φ and the angle γ between the X-ray and the line connecting the X-ray source and origin O . Considering the Taylor series approximation, the projection $I(\varphi, \gamma)$ and its reverse projection $I(\varphi + \pi + 2\gamma, -\gamma)$ can be expressed as

$$I(\varphi, \gamma) = I_R(\varphi, \gamma) \cdot [S_{\omega_g = p_2/4R_2} + \theta(\varphi, \gamma) \cdot S'_{\omega_g = p_2/4R_2}]$$

and

$$I(\varphi + \pi + 2\gamma, -\gamma) = I_R(\varphi + \pi + 2\gamma, -\gamma) \cdot [S_{\omega_g = p_2/4R_2} + \theta(\varphi + \pi + 2\gamma, -\gamma) \cdot S'_{\omega_g = p_2/4R_2}]. \quad (8)$$

Obviously, the beams (φ, γ) and $(\varphi + \pi + 2\gamma, -\gamma)$ have the same propagation path and the opposite propagation direction, respectively [25], which can be displayed in Fig. 2. Thus, we have the following two relationships:

$$I_R(\varphi, \gamma) = I_R(\varphi + \pi + 2\gamma, -\gamma)$$

and

$$\theta(\varphi, \gamma) = -\theta(\varphi + \pi + 2\gamma, -\gamma). \quad (9)$$

Under the condition of Eq. (9), the refraction angle $\theta(\varphi, \gamma)$ can be achieved by solving the two eqnarrays in Eq. (8):

$$\theta(\varphi, \gamma) = \frac{S_{\omega_g = p_2/4R_2} I(\varphi, \gamma) - I(\varphi + 2\gamma + \pi, -\gamma)}{S'_{\omega_g = p_2/4R_2} I(\varphi, \gamma) + I(\varphi + 2\gamma + \pi, -\gamma)}. \quad (10)$$

Eq. (10) can be seen as the fan-beam version of the RP method. It is worth mentioning that the X-ray source should rotate 360° around the center in the RP method. If this requirement cannot be satisfied, the PR-method will be invalid and the PS-method is recommended. Comparing with the refraction angle θ , we are more eager to obtain the refraction index decrement δ from

refraction angle data. In the following section, we discuss how to obtain the refractive index decrement δ under the fan-beam scanning model.

3. Reconstruction algorithms

In this section, the 2D Katsevich formulae [34–37] are described. After that, an implementation strategy of these formulae for fan-beam DPC-CT is provided. Finally, we compare the implementations of our algorithm with other algorithms for DPC-CT.

3.1. 2D Katsevich formulae

Katsevich's formula is based on the conception of PI-line, which is a straight line connecting two points on the source trajectory as shown in Fig. 3. According to Katsevich's theory, for a given PI-line, the refractive index decrement value δ of the point x in this PI-line can be reconstructed from its radon transform:

$$\delta(\mathbf{x}) = \frac{1}{2\pi^2} \int_{\lambda_1}^{\lambda_2} \frac{d\varphi}{|\mathbf{x} - \mathbf{c}(\varphi)|} \int_{-\pi}^{\pi} \left(\frac{\partial \Theta(\varphi, \gamma)}{\partial \varphi} - \frac{\partial \Theta(\varphi, \gamma)}{\partial \gamma} \right) \frac{d\gamma}{\sin(\tilde{\gamma} - \gamma)}, \quad (11)$$

where $\Theta(\varphi, \gamma)$ is the radon transform of the refractive index decrement δ along the X-ray propagation path, and represents the angle between the X-ray passing through the point x and the X-ray passing through the origin O . Obviously, the PI-line segment divides the source trajectory into two angular ranges. There are $\lambda_1 \leq \varphi \leq \lambda_2$ and $\lambda_2 \leq \varphi \leq \lambda_1 + 2\pi$, which are equivalent and independent for back-projection. Therefore, the back-projection process of Eq. (11) can also be performed on the angular ranges: $\lambda_2 \leq \varphi \leq \lambda_1 + 2\pi$. If both the angular ranges are considered, the reconstruction formula can be rewritten as

$$\delta(\mathbf{x}) = \frac{1}{4\pi^2} \int_0^{2\pi} \frac{d\varphi}{|\mathbf{x} - \mathbf{c}(\varphi)|} \int_{-\pi}^{\pi} \left(\frac{\partial \Theta(\varphi, \gamma)}{\partial \varphi} - \frac{\partial \Theta(\varphi, \gamma)}{\partial \gamma} \right) \frac{d\gamma}{\sin(\tilde{\gamma} - \gamma)}. \quad (12)$$

Although the refraction-angle data can be generated from the Talbot interferometry, the radon transform $\Theta(\varphi, \gamma)$ is difficult to obtain. Thus, Eqs. (11) and (12) cannot be implemented for fan-beam DPC-CT unless some changes are made.

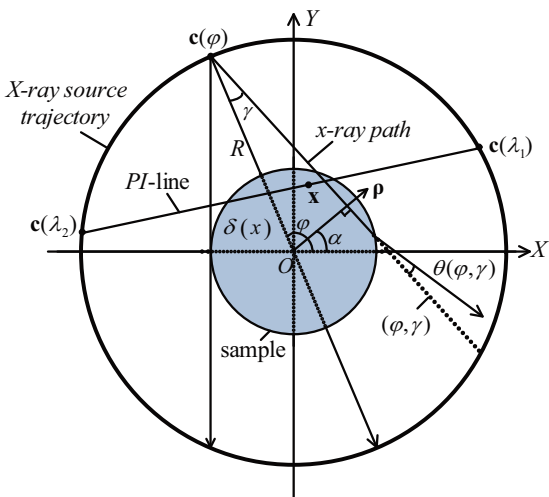


Fig. 2. Geometry of reverse projection in fan-beam case. The X-ray source moves around the sample along a circle trajectory of radius R . The source position depends on source rotation angle φ and radius R and can be defined as $\mathbf{c}(\varphi) = (R \cos \varphi, R \sin \varphi)$. Each X-ray beam can be labeled by (φ, γ) and its reverse projection can be specified by $(\varphi + \pi + 2\gamma, -\gamma)$.

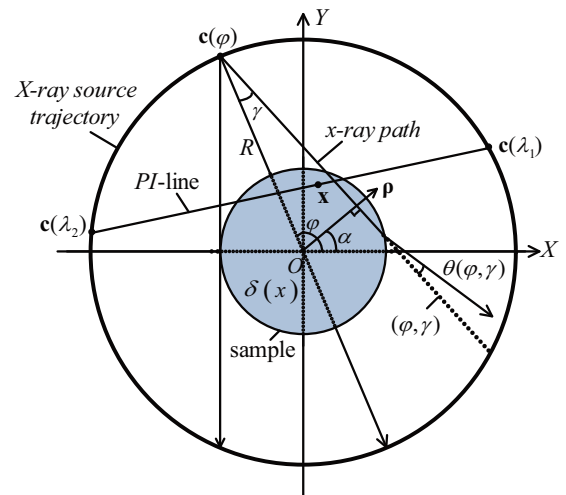


Fig. 3. Illustration of PI-line. The PI-line intersect the X-ray source trajectory at two points $\mathbf{c}(\lambda_1)$ and $\mathbf{c}(\lambda_2)$. λ_1 and λ_2 are the angular parameters of the two points. The vector ρ is perpendicular to the X-ray path. The angle α is the angle difference between the vector ρ and x-axis.

3.2. Implementation strategy

It is well known that the refraction angle only depends on the gradients of refractive index decrement δ in the direction ρ :

$$\theta(\varphi, \gamma) = \int_l \frac{\partial \delta(x, y)}{\partial \rho} dl = \frac{d\Theta(\varphi, \gamma)}{d\rho}, \quad (13)$$

where ρ denotes the vector perpendicular to the X-ray path, $\Theta(\varphi, \gamma)$ is the radon transform of the refractive index decrement δ along the X-ray propagation path. From the geometrical model shown in Fig. 3, it is easy to work out the following two equations:

$$\rho = R \sin \gamma \Rightarrow d\rho = R \cos \gamma d\gamma$$

and

$$\gamma + \varphi - \alpha = \frac{\pi}{2} \Rightarrow \frac{\partial \varphi}{\partial \gamma} = -1. \quad (14)$$

Under the condition of Eq. (14), the refraction angle $\theta(\varphi, \gamma)$ can be expressed by the derivative of the line integrals $\Theta(\varphi, \gamma)$ with

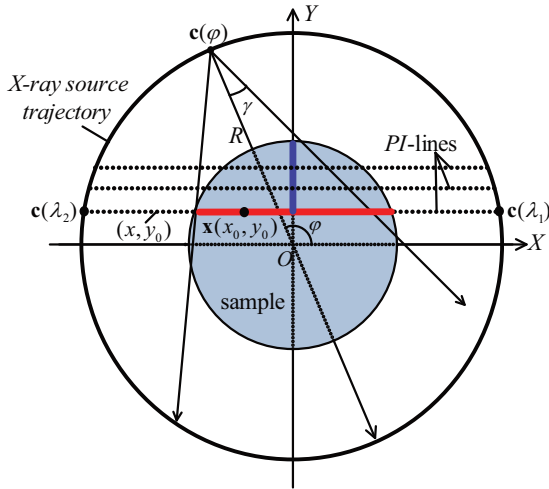


Fig. 4. Geometrical model of the PI-lines are parallel to the x-axis. The PI-line intersect the X-ray source trajectory at two points $c(\lambda_1)$ and $c(\lambda_2)$. Each point x on the PI-line can be specified by the coordinates (x, y_0) , where y_0 is the ordinate of all the points on the PI-line. (For interpretation of the references to color in this figure caption, the reader is referred to the web version of this paper.)

respect to the angle γ

$$\begin{aligned} \theta(\varphi, \gamma) &= \frac{d\Theta(\varphi, \gamma)}{d\rho} = \frac{1}{R \cos \gamma} \frac{d\Theta(\varphi, \gamma)}{d\gamma} \\ &= \frac{1}{R \cos \gamma} \left(\frac{\partial \Theta(\varphi, \gamma)}{\partial \varphi} \frac{\partial \varphi}{\partial \gamma} + \frac{\partial \Theta(\varphi, \gamma)}{\partial \gamma} \right) \\ &= \frac{-1}{R \cos \gamma} \left(\frac{\partial \Theta(\varphi, \gamma)}{\partial \varphi} - \frac{\partial \Theta(\varphi, \gamma)}{\partial \gamma} \right). \end{aligned} \quad (15)$$

Eq. (15) is essentially the same as Eq. (9) in [25]. Although the radon transform $\Theta(\varphi, \gamma)$ cannot be measured by Talbot interferometry, the refraction angle $\theta(\varphi, \gamma)$ can be easily converted to the derivative data $\partial \Theta(\varphi, \gamma) / \partial \varphi - \partial \Theta(\varphi, \gamma) / \partial \gamma$ employed in Katsevich's algorithm by multiplying the factor $-R \cos \gamma$. Thus, the implementation of Eqs. (11) and (12) for fan-beam DPC-CT can be illustrated as

$$\delta(\mathbf{x}) = \frac{-1}{2\pi^2} \int_{\lambda_1}^{\lambda_2} \frac{d\varphi}{|\mathbf{x} - \mathbf{c}(\varphi)|} \int_{-\pi}^{\pi} R \cos \gamma \theta(\varphi, \gamma) \frac{d\gamma}{\sin(\tilde{\gamma} - \gamma)} \quad (16)$$

$$\delta(\mathbf{x}) = \frac{-1}{4\pi^2} \int_0^{2\pi} \frac{d\varphi}{|\mathbf{x} - \mathbf{c}(\varphi)|} \int_{-\pi}^{\pi} R \cos \gamma \theta(\varphi, \gamma) \frac{d\gamma}{\sin(\tilde{\gamma} - \gamma)}. \quad (17)$$

Eq. (16) means that the value of refractive index decrement δ at the point \mathbf{x} can be exactly reconstructed from the refraction angle data that belong to angular ranges $\lambda_1 \leq \varphi \leq \lambda_2$. In other words, the truncation of the refraction angle data that belong to angular ranges $\lambda_2 \leq \varphi \leq \lambda_1 + 2\pi$ would not affect the reconstruction of $\sigma(\mathbf{x})$. It is feasible to choose Eq. (17) under the complete refraction angle data condition.

Table 1
Geometrical configuration.

Parameters	Values
X-ray source trajectory radius (mm)	500
The number of source positions	1440
The scanning step angle	0.25°
The X-ray source rotation angle range	0–360°
The full fan angle	20°
The resolution of the phantom	512 × 512
Field of view (mm)	120
The number of equi-angular rays at each source position	512

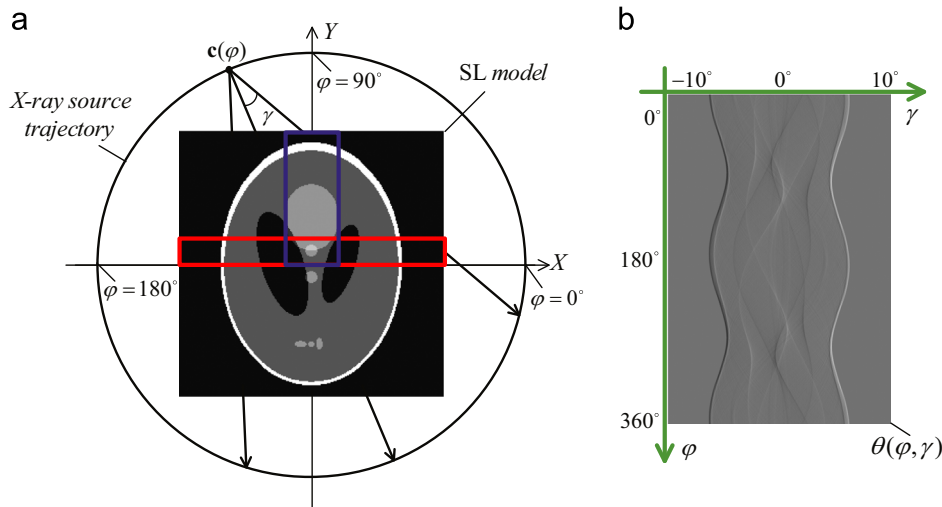


Fig. 5. (a) Scanning model. The regions specified by the rectangles will be chosen to be reconstructed in the next part. (b) The complete refraction angle data set is shown by the DPC sinogram. (For interpretation of the references to color in this figure caption, the reader is referred to the web version of this paper.)

3.3. Comparison with the BPF algorithm

The implementation of the BPF algorithm for fan-beam DPC-CT [28,29] was, firstly, studied by Chen and Qi, which is also based on the conception of PI-line. Here, we use the PI-lines which are parallel to the x -axis to illustrate their work. According to their work, the reconstruction of the refractive index decrement δ of the point x on the PI-line shown in Fig. 4 mainly includes two steps: back-projection and filtering. The back-projection process requires all the refraction-angle $\theta(\varphi, \gamma)$ in the angle range $\lambda_1 \leq \varphi \leq \lambda_2$ to be back-projected to the PI-line which contains the point $X(x_0, y_0)$ and provides an intermediate

result

$$B(x, y_0) = \int_{\lambda_1}^{\lambda_2} \frac{R \cos \gamma \theta(\varphi, \gamma)}{|\mathbf{x}(x, y_0) - \mathbf{c}(\varphi)|} d\varphi. \quad (18)$$

Under the complete refraction angle data condition, this process can also be performed according to the following equation:

$$B(x, y_0) = \frac{1}{2} \left(\int_{\lambda_1}^{\lambda_2} - \int_{\lambda_2}^{\lambda_1 + 2\pi} \right) \frac{R \cos \gamma \theta(\varphi, \gamma)}{|\mathbf{x}(x, y_0) - \mathbf{c}(\varphi)|} d\varphi. \quad (19)$$

The filtering-process is performed on the intermediate result $B(x, y_0)$ to calculate the value of refractive index decrement δ of

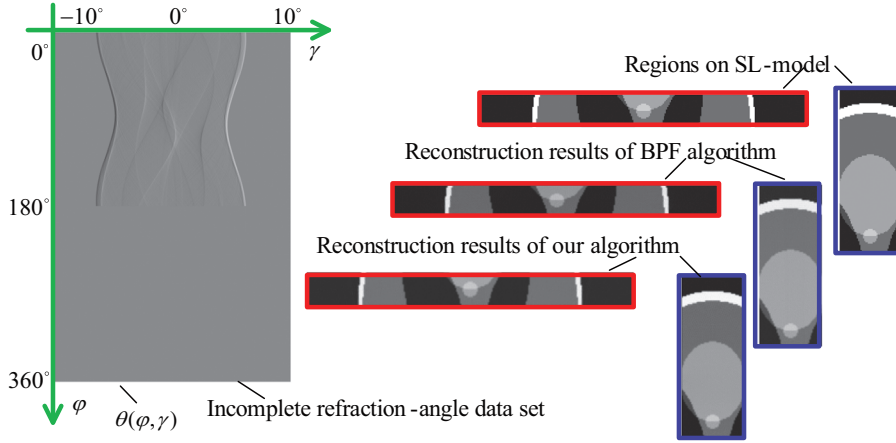


Fig. 6. Incomplete reconstructions generated from the Shepp-Logan model by different algorithms.

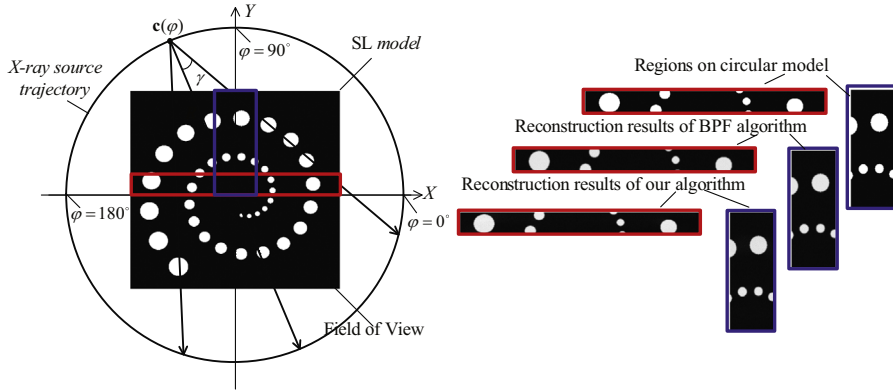


Fig. 7. Incomplete reconstructions generated from the circular model by different algorithms. (For interpretation of the references to color in this figure caption, the reader is referred to the web version of this paper.)

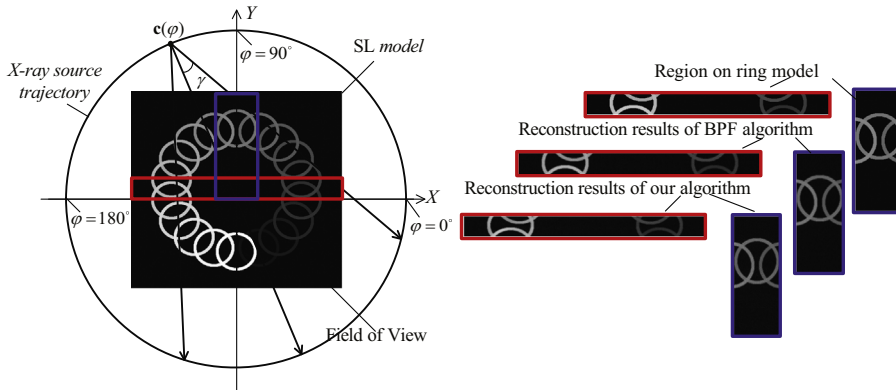


Fig. 8. Incomplete reconstructions generated from the ring model by different algorithms. (For interpretation of the references to color in this figure caption, the reader is referred to the web version of this paper.)

the point $X(x_0, y_0)$:

$$\delta(x_0, y_0) = \frac{-1}{2\pi} \int_{-\infty}^{\infty} \frac{B(x, y_0)}{x - x_0} dx. \quad (20)$$

This step is usually carried out by using the *Truncated Hilbert Transform* (THT) [28,39] or the *Singular Value Decomposition* (SVD) [40]. Obviously, the Katsevich formula filters the refraction angle data directly, while the BPF algorithm filters the data on the intermediate result $B(x, y_0)$. This difference leads to different efficiencies in dealing with different-shape areas under the incomplete refraction angle data condition.

Now, we assume that the refraction angle data $\theta(\varphi, \gamma)$ in the angle range $\lambda_2 \leq \varphi \leq \lambda_1 + 2\pi$ are truncated. In this situation, only the points above the PI-line determined by the two points $c(\lambda_1)$ and $c(\lambda_2)$ can be exactly reconstructed. When the value of δ on the red segment shown in Fig. 4 is considered, the BPF algorithm will backproject all the refraction angle data $\theta(\varphi, \gamma)$ to the PI-line which contains the red segment and then the filtering-process is shown in Eq. (20). Similarly, the Katsevich algorithm filters all these refraction angle data and then backprojects all of them to this PI-line. The amount of performing the filtering-process required by the BPF algorithm is only one, while that required by the Katsevich algorithm grows with the number of source positions $c(\varphi)$. Thus, the BPF algorithm may be faster than the Katsevich algorithm. When reconstructing the blue segment displayed in Fig. 4, the Katsevich algorithm requires that all the refraction angle data are filtered and then backprojected to the blue segment. To reconstruct the blue segment displayed in Fig. 4, the BPF algorithm requires that all the refraction angle data are back-projected to all the PI-lines passing through the blue segment, and then the filtering-process shown in Eq. (20) is performed for all the PI-lines one by one. In this case, the Katsevich algorithm may be faster than BPF algorithm. This is because less back-projection operation is required by the Katsevich algorithm compared with the BPF algorithm. The above conclusions will be demonstrated by numerical simulations in the next section. In this paper, the implementation strategy of Katsevich algorithm for fan-beam DPC-CT can be summarized in Algorithm 1.

Algorithm 1. The implementation strategy of Katsevich algorithm for

Input: a given point x , the origin O , the angle γ .

- (1) PI line determination: For a given point x , there must be a unique PI-line which can be specified by the initial and final angular parameters λ_1 and λ_2 which could be calculated by some numerical methods [42].
- (2) Weighting computing: according to Eq. (16), a similar cosine-weighting operation on fan-beam refraction-angle projection is computed as $g(\varphi, \gamma) = R \cos \gamma \theta(\varphi, \gamma)$.
- (3) Filtering processing: The cosine-weighted data $g(\varphi, \gamma)$ is convolved with a one-dimensional filter $1/\sin \gamma$ along PI line and the filtered data is $g'(\varphi, \gamma) = \int_{\lambda_1}^{\lambda_2} g(\varphi, \gamma) * (1/\sin \gamma) d\gamma$. Where the symbol $*$ denotes convolution operation.
- (4) Weighted backprojection: The filtered data multiplied by the distance weighting factor $|x - c(\varphi)|$ are back-projected to the point x to obtain the refractive index decrement $\delta(x) = (-1/2\pi^2) \int_{\lambda_1}^{\lambda_2} d\varphi / |x - c(\varphi)| \int_{-\pi}^{\pi} R \cos \gamma \theta(\varphi, \gamma) d\gamma / \sin(\tilde{\gamma} - \gamma)$.

Output: the refractive index decrement $\delta(x) = (-1/2\pi^2) \int_{\lambda_1}^{\lambda_2} (d\varphi / |x - c(\varphi)|) \int_{-\pi}^{\pi} R \cos \gamma \theta(\varphi, \gamma) d\gamma / \sin(\tilde{\gamma} - \gamma)$.

4. Numerical simulations and discussion

In this section, we carry out numerical simulations to display the performances of our method. This section includes three parts. In the first part, the experimental environment and geometrical configurations are introduced. In the second part, the conclusions of Section 3.3 are demonstrated. In the third part, the influence of the approximation errors introduced by the RP-method on our algorithm is analyzed and discussed.

Table 2

CPU times of our algorithm and BPF algorithm for fan-beam DPC-CT.

Reconstruction area	Our algorithm	BPF algorithm
Red area		
Filtering time	11.9 s	0.7 s
Back-projecting time	25.8 s	25.8 s
Blue area		
Filtering time	11.9 s	3.3 s
Back-projecting time	25.3 s	128.7 s

Table 3

PSNR and entropy results of the reconstructed image generated from the Shepp–Logan model by different algorithms.

Reconstruction area	BPF algorithm	Our algorithm
Red area		
PNSR	25.72	26.07
Entropy	4.59	5.33
Blue area		
PNSR	25.15	25.83
Entropy	4.96	5.84

Table 4

PSNR and entropy results of the reconstructed image generated from the circular model by different algorithms.

Reconstruction area	BPF algorithm	Our algorithm
Red area		
PNSR	22.23	22.83
Entropy	4.09	3.67
Blue area		
PNSR	23.11	23.05
Entropy	3.92	3.39

4.1. Experimental environment and geometrical configuration

All the numerical simulations are implemented in a MATLAB environment on a modern desktop computer (Inter Pentium Dual E2160 CPU and 2 GB RAM) to test the performance of the proposed

algorithm. The standard *Shepp–Logan* (SL) phantom shown in Fig. 5 was employed to represent the refractive index decrement distribution. The parameters of the geometrical configuration of this experiment are displayed in Table 1.

The refraction angle $\theta(\varphi, \gamma)$ for each X-ray was analytically calculated according to Snell's law:

$$\theta(\varphi, \gamma) = \int_{l: x\text{-ray path}} \frac{\partial \delta}{\partial x} \sin(\varphi + \gamma) - \frac{\partial \delta}{\partial y} \cos(\varphi + \gamma) dl. \quad (21)$$

Table 5
PSNR and entropy results of the reconstructed image generated from the ring model by different algorithms.

Reconstruction area	BPF algorithm	Our algorithm
Red area		
PNSR	24.77	25.13
Entropy	4.25	4.05
Blue area		
PNSR	25.30	25.35
Entropy	4.31	4.02

The partial derivatives in Eq. (21) were directly calculated by the two-point differential method. The complete refraction-angle data set is shown in Fig. 5(b).

4.2. Reconstruction and comparison results

In this subsection, the numerical simulations are carried out on the incomplete refraction data set shown in Figs. 6–8, which is obtained by truncating the refraction angle data $\theta(\varphi, \gamma)$ in the angle range $\pi \leq \varphi \leq 2\pi$ from the complete data set. Only the

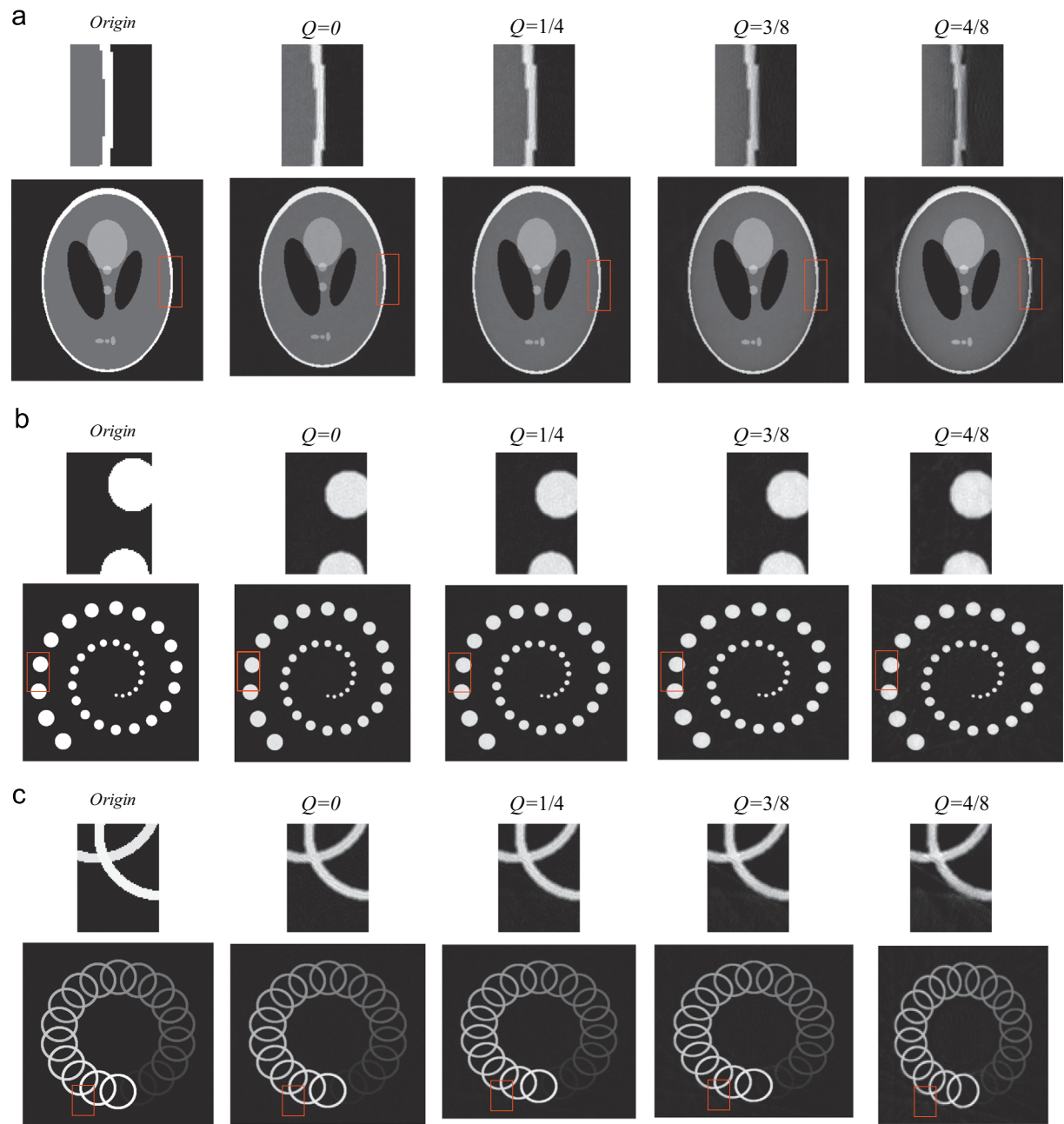


Fig. 9. Different reconstruction images under the ideal condition. $Q=0$ means that the refraction-angle data are extracted without any errors and our algorithm is performed under ideal condition. The small rectangular windows were enlarged to display the artifacts. (a) Original and reconstructed images of the Shepp-Logan model under the ideal condition, (b) Original and reconstructed images of the Circular model under the ideal condition and (c) Original and reconstructed images of the Ring model under the ideal condition.

regions specified by the red and blue rectangles in Figs. 5, 7 and 8 are chosen to be reconstructed. The two rectangles are defined by the pixel coordinates of their upper left and lower right corners. For red rectangles, these are (1,207) and (512,256). For blue rectangles, these are (207,1) and (306,256). The numbers of the points in the two rectangles are the same, which are both 25 600. Our algorithm and BPF algorithm were performed to reconstruct these points. The implantation of the filtering-process of BPF algorithm denoted in Eq. (20) was carried out by using the Truncated Hilbert Transform. The reconstruction results of these algorithms are displayed in Fig. 6. To assess the computation times

of filtering step and back-projecting step, the CPU times of our algorithm and the BPF algorithm are shown in Table 2. For the red rectangle, the BPF algorithm is faster than our algorithm, since the amount of performing the filtering-process required by the BPF algorithm is less than that of our algorithm. For the blue rectangle, our algorithm is faster than the BPF algorithm, because the BPF algorithm consumes too much more time on the back-projection process. The reasons for this phenomenon have already been analyzed in Section 3.3. For the different reconstructed models in the experiments, *Peak Signal to Noise Ratio* (PSNR) and Entropy [1] indices are adopted to objectively evaluate the quality of the

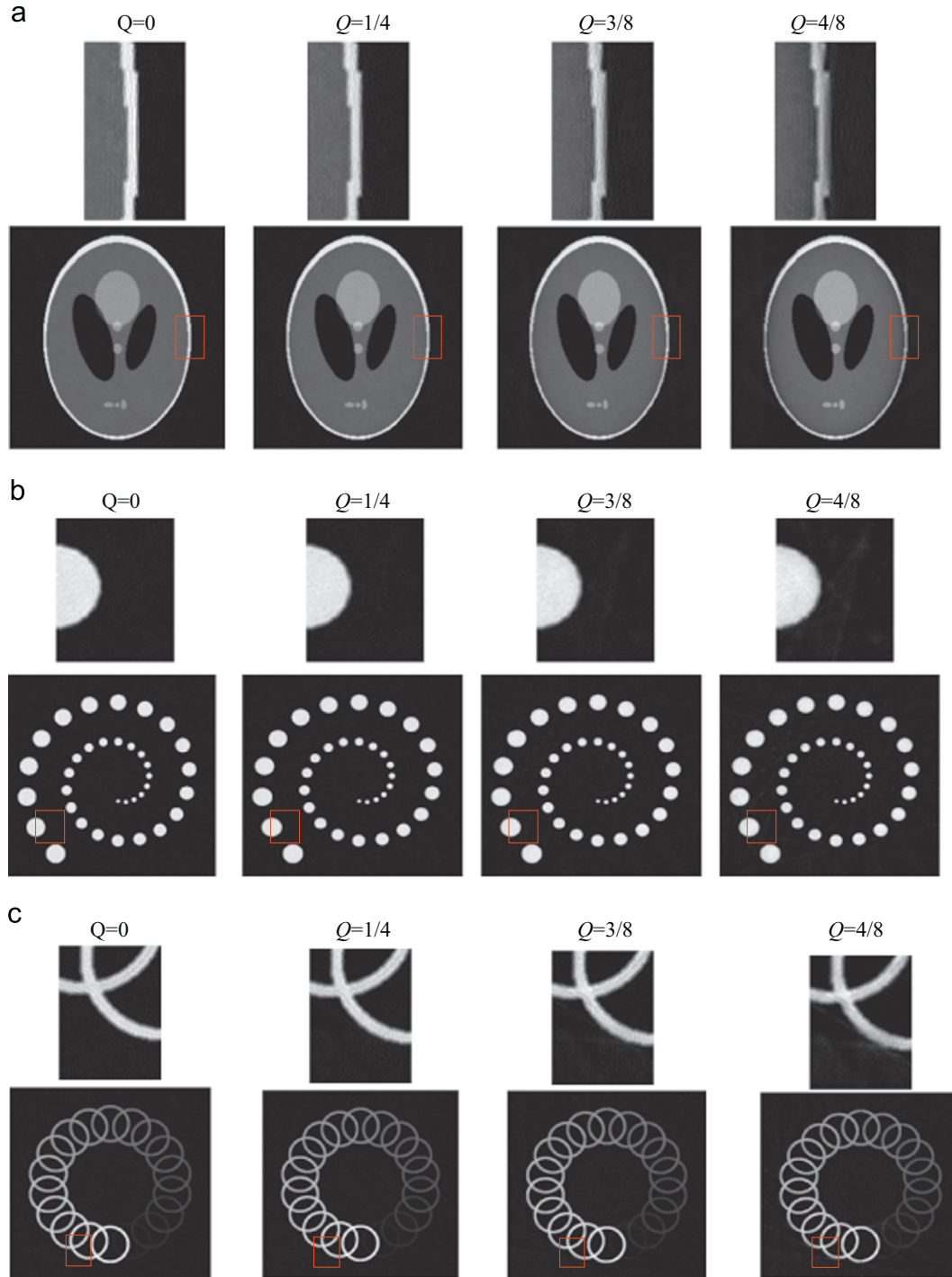


Fig. 10. Different reconstruction images under the noisy condition. $Q=0$ means that the refraction-angle data are extracted without any errors and our algorithm is performed under the noisy condition. The small rectangular windows were enlarged to display the artifacts.

reconstructions. The numerical results of different algorithms are summarized in Tables 3–5. It can be seen from Tables 3–5 that when PSNR results of different reconstructions decrease, the corresponding Entropy results of different reconstructions will increase. This is because smaller PSNR results may produce unsatisfactory experimental results, which leads to the significant increase in the reconstructed error and artifacts. In this case, the corresponding entropy value will increase significantly due to the effects of the artifacts. From Tables 3–5, it is obvious that our algorithm can obtain better performance compared with the BPF algorithm.

4.3. Influence of the approximation errors

According to Eq. (7), since the Taylor series approximation is employed, the RP-method will inevitably introduce some approximation errors. Are they fatal? When are, and when are not? Here, we intend to give a semi-quantitative answer about these questions by several numerical simulations. The main reason why the Taylor series approximation is used, I think, is that the analytical and accurate expression of the shifting curve function S has not been achieved. Thus, the exact refraction angle data can be obtained unless some approximations such as the Taylor series approximation are employed. However, some papers [26] adopt Eq. (22) to describe the shifting curve function S near its half-slope position:

$$S(\theta) \approx a + b \sin\left(\frac{2\pi D}{p_2} \theta\right), \quad (22)$$

where a and b are constant numbers which can be determined by experimental methods [17,18], D is the distance between the phase-grating G_1 and the mask grating G_2 , p_2 is the period of the grating G_2 . In this paper, we assume that Eq. (22) is accurate enough, on which our semi-quantitative answer is basing. Substitute Eq. (9) with Eq. (22) and then solve the refraction-angle from the two equations shown in Eq. (8), we have the relationship between the approximate value θ^* and true value θ of the refraction angle:

$$\theta^* = \theta \frac{\sin\left(\frac{2\pi D}{p_2} \cdot \theta\right)}{\frac{2\pi D}{p_2} \cdot \theta}. \quad (23)$$

Obviously, the refraction angle data precision depends on the product of its value and the parameter D/p_2 . For DPC-CT reconstruction, we defined the parameter Q to describe this relation:

$$Q = \frac{D}{p_2} \theta_{\max}, \quad (24)$$

where θ_{\max} denotes the maximum value in refraction angle data set. For the experimental results from different models in this subsection, we demonstrate and validate the effect of the relationship on DPC-CT reconstruction. It is shown in Figs. 9 and 10 that different images reconstructed suffer from the different artifacts under the “ideal” and “noisy” condition. For each model, we will calculate the approximate values of the refraction angle data according to Eq. (23) with different values Q and reconstruct the model by using these approximate refraction angle values. In addition, Peak Signal to Noise Ratio (PSNR) and Entropy [1] indices are adopted to objectively evaluate the quality of the reconstructions. Under the “noisy” condition, additive Gaussian noise with standard deviation 0.1 of the maximum value of the generated projection is added to the projection data. In Figs. 9 and 10, the Shepp–Logan-model, the circular model and the ring model were employed to study the effect of this relationship of DPC-CT reconstruction under the ideal and noisy conditions.

Table 6

PSNR and Entropy of the reconstructions under the ideal condition. For each reconstruction, we have two rows. The first row is PSNR, the second row is Entropy.

Model	$Q=0$	$Q=1/4$	$Q=3/8$	$Q=4/8$
Shepp_Logan				
PSNR	25.27	24.94	23.29	21.87
Entropy	4.54	4.73	5.03	5.38
Circular				
PSNR	24.49	23.98	23.12	22.51
Entropy	3.41	3.44	3.56	3.75
Ring				
PSNR	24.78	24.51	23.99	23.11
Entropy	4.01	4.07	4.11	4.17

Table 7

PSNR and Entropy of the reconstructions under the noisy condition. For each reconstruction, we have two rows. The first row is PSNR, the second row is Entropy.

Model	$Q=0$	$Q=1/4$	$Q=3/8$	$Q=4/8$
Shepp_Logan				
PSNR	24.52	24.23	23.33	21.65
Entropy	4.76	5.23	5.62	5.80
Circular				
PSNR	23.48	23.35	22.72	22.23
Entropy	3.84	4.25	4.49	4.76
Ring				
PSNR	24.18	24.10	23.59	22.72
Entropy	4.51	4.76	4.87	4.91

Tables 6 and 7 show the PSNR and entropy indices of different reconstructions by using different Q from Eq. (24) under the “ideal” and “noisy” conditions. From Tables 6 and 7, the artifacts caused by the approximation are not visually manifest when Q varies from 0 to 1/4. When Q increases from 1/4 to 3/8, the reconstructions are still not visually very bad. However, the performance of reconstructions may largely degrade when Q exceeds 3/8. This is because when Q varies significantly, the approximation error of Taylor series will be larger, which degrades the performance of image reconstruction.

Based on above numerical simulations, we worked out our semi-quantitative answer that the RP-method can provide accurate enough data for our reconstruction algorithm, if all the refraction angles are smaller than $p_2/4D$. In fact, Zhu et al. have pointed out that the RP-method is not very sensitive to large refraction angles, because the shifting curve is saturated when the refraction angles are larger than $p_2/4D$ [25]. For DPC-CT reconstruction, large refraction angles usually occupy only a small part of all the refraction-angle data set. Thus, even if a few refraction angles are larger than $p_2/4D$, the reconstruction may be still acceptable. Of course, if Eq. (22) was proved to be really more accurate than the linear approximation, we would rewrite Eq. (10) as

$$\theta(\varphi, \gamma) = \frac{p_2}{2\pi D} \arcsin \frac{aI(\varphi, \gamma) - I(\varphi + 2\gamma + \pi, -\gamma)}{bI(\varphi, \gamma) + I(\varphi + 2\gamma + \pi, -\gamma)}. \quad (25)$$

5. Conclusions

In differential phase contrast CT, the phase shift is exploited as the imaging signal to offer more details regarding the internal structure. In this paper, DPC-CT reconstruction problems in fan-beam geometry are studied. To obtain desired reconstruction performance, the Reverse-Projection (RP) method is exploited to extract the refraction-angle data efficiently and a Katsevich-type

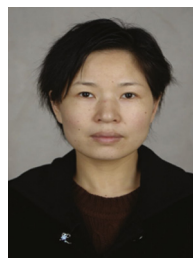
formula is presented for fan-beam DPC-CT reconstruction. Numerical simulations are provided to evaluate the influence of the approximation errors introduced by the different algorithms. Our simulation results indicate that the proposed algorithm does have better stability over the BPF algorithm.

Acknowledgment

This work is supported by the National Natural Science Foundation of China (Grant nos.: 61300142, 61105051 and 61100079).

References

- [1] M. Yang, J. Pan, J. Zhang, S. Song, F. Meng, X. Li, D. Wei, Center of rotation automatic measurement for fan-beam CT system based on sinogram image features, *Neurocomputing* 120 (2013) 250–257.
- [2] S. Murala, Q. Wu, Local ternary co-occurrence patterns: a new feature descriptor for MRI and CT image retrieval, *Neurocomputing* 119 (2013) 399–412.
- [3] R. Ye, X. Lu, H. Liu, Local tomography based on grey model, *Neurocomputing* 101 (2013) 10–17.
- [4] U. Bonse, X-ray imaging: past and present, in: *Proceedings of SPIE*, 2008, pp. 707801–707802.
- [5] U. Bonse, M. Kart, An x-ray interferometry with long interfering beam paths, *Appl. Phys. Lett.* 7 (1965) 99–101.
- [6] A. Momose, T. Takeda, Y. Itai, et al., Phase-contrast X-ray computed tomography for observing biological soft tissues, *Nat. Med.* 2 (1996) 473–475.
- [7] A. Yoneyama, T. Takeda, Y. Tsuchiya, et al., Coherence-contrast X-ray imaging based on X-ray interferometry, *Appl. Opt.* 44 (16) (2005) 3258–3601.
- [8] A. Snigirev, I. Snigireva, V. Kohn, On the possibilities of X-ray phase contrast microimaging by coherent high-energy synchrotron radiation, *Rev. Sci. Instrum.* 66 (12) (1995) 5486–5492.
- [9] S. Wilkins, T. Gureyev, D. Gao, et al., Phase-contrast imaging using polychromatic hard X-rays, *Nature* 384 (28) (1996) 335–338.
- [10] P. Spanne, C. Raven, A. Snigirev, et al., In-line holography and phase-contrast microtomography with high energy X-rays, *Phys. Med. Biol.* 44 (1999) 741–749.
- [11] T. Davis, D. Gao, T. Gureyev, et al., Phase-contrast imaging of weakly absorbing materials using hard X-rays, *Nature* 373 (16) (1995) 595–598.
- [12] D. Chapman, W. Thomlinson, R. Johnston, et al., Diffraction enhanced X-ray imaging, *Phys. Med. Biol.* 42 (1997) 2015–2025.
- [13] F. Dilmanian, Z. Zhong, B. Ren, et al., Computed tomography of X-ray index of refraction using the diffraction enhanced imaging method, *Phys. Med. Biol.* 45 (2000) 933–946.
- [14] T. Weitkamp, A. Diaz, C. David, et al., X-ray phase imaging with a grating interferometer, *Opt. Express* 13 (16) (2005) 6296–6304.
- [15] C. David, B. Nohammer, H. Solak, Differential X-ray phase contrast imaging using a shearing interferometer, *Appl. Phys. Lett.* 81 (17) (2007) 3287.
- [16] A. Momose, S. Kawamoto, I. Koyama, et al., Demonstration of X-ray Talbot interferometer, *Jpn. J. Appl. Phys.* 42 (2003) 866–868.
- [17] F. Pfeiffer, T. Weitkamp, O. Bunk, et al., Phase retrieval and differential phase-contrast imaging with low-brilliance X-ray sources, *Nat. Phys.* 2 (2006) 258–261.
- [18] F. Pfeiffer, M. Bech, O. Bunk, et al., Hard X-ray dark-field imaging using a grating interferometer, *Nat. Mater.* 7 (2008) 134–137.
- [19] Z. Huang, K. Kang, L. Zhang, et al., Alternative method for differential phase-contrast imaging with weakly coherent hard X rays, *Phys. Rev. A* 79 (2009) 013815.
- [20] R. Zhang, Z. Chen, Z. Huang, et al., Monte Carlo simulation of grating-based neutron phase contrast imaging at CPHS, *Nucl. Instrum. Methods Phys. Rev. A* 79 (2011) 013815.
- [21] V. Revol, C. Kottler, R. Kaufmann, et al., X-ray interferometer with bent gratings: towards larger fields of view, *Nucl. Instrum. Methods Phys. Res. A* 648 (21) (2010) 302–305.
- [22] C. David, T. Weitkamp, F. Pfeiffer, Hard x-ray phase imaging and tomography using a grating interferometer, *Spectrochim. Acta B* 62 (2007) 626–630.
- [23] M. Bech, T. Jensen, R. Feidenhans, Soft-tissue phase-contrast tomography with an X-ray tube source, *Phys. Med. Biol.* 54 (2009) 2747–2753.
- [24] F. Pfeiffer, C. David, O. Bunk, Region-of-interest tomography for grating-based X-ray differential phase-contrast imaging, *Phys. Rev. Lett.* 101 (2008) 168101.
- [25] P. Zhu, K. Zhang, Z. Wang, Low-dose, simple, and fast grating-based X-ray phase contrast imaging, *Proc. Natl Acad. Sci.* 107 (2011) 13576–13581.
- [26] I. Jerjen, V. Revol, C. Kottler, et al., Phase contrast cone beam tomography with an X-ray grating interferometer, in: *International Conference on Advanced Phase Measurement Methods in Optics and Imaging*, vol. 1236, 2010, pp. 227–231.
- [27] Z. Qi, P. Lauzier, N. Bevin, et al., Helical X-ray differential phase contrast computed tomography, in: *Proceedings of SPIE*, vol. 7961, 2011, p. 79611Q.
- [28] G. Chen, Z. Qi, Image reconstruction for fan-beam differential phase contrast computed tomography, *Phys. Med. Biol.* 53 (2008) 1015–1025.
- [29] J. Fu, P. Li, Q. Wang, et al., A reconstruction method for equidistant fan beam differential phase contrast computed tomography, *Phys. Med. Biol.* 56 (2011) 4529–4538.
- [30] F. Noo, R. Clackdoyle, J. Pack, A two-step Hilbert transform method for 2D image reconstruction, *Phys. Med. Biol.* 49 (2004) 3903–3923.
- [31] Y. Zou, X. Pan, Exact image reconstruction on PI-lines from minimum data in helical cone-beam CT, *Phys. Med. Biol.* 49 (2004) 941–959.
- [32] X. Pan, Y. Zou, D. Xia, Image reconstruction in peripheral and central regions-of-interest and data redundancy, *Med. Phys.* 32 (2005) 673–684.
- [33] E. Sidky, Y. Zou, X. Pan, Minimum data image reconstruction algorithms with shift-invariant filtering for helical cone-beam CT, *Phys. Med. Biol.* 50 (2005) 1643–1657.
- [34] A. Katsevich, Theoretically exact filtered-backprojection type inversion algorithm for spiral CT, *SIAM J. Appl. Math.* 62 (2002) 2012–2026.
- [35] F. Noo, M. Defrise, R. Clackdoyle, et al., Image reconstruction from fan-beam projections on less than a short scan, *Phys. Med. Biol.* 47 (2002) 2525–2546.
- [36] F. Noo, S. Hoppe, F. Dennerlein, et al., A new scheme for view-dependent data differentiation in fan-beam and cone-beam computed tomography, *Phys. Med. Biol.* 52 (2007) 5393–5414.
- [37] A. Faridani, R. Hass, D. Solmon, Numerical and theoretical explorations in helical and fan-beam tomography, *J. Phys.: Conf. Ser.* 124 (2008) 012024.
- [38] T. Donath, M. Chabior, F. Pfeiffer, Inverse geometry for grating-based X-ray phase-contrast imaging, *J. Appl. Phys.* 106 (2009) 0547031–0547037.
- [39] M. Defrise, F. Noo, R. Clackdoyle, Truncated Hilbert transform and image reconstruction from limited tomographic data, *Inverse Probl.* 22 (2006) 1037–1053.
- [40] H. Yu, Y. Ye, W. Ge, Interior reconstruction using the truncated Hilbert transform via singular value decomposition, *J. X-Ray Sci. Technol.* 16 (2008) 243–251.
- [41] P. Lauzier, Z. Qi, J. Zambelli, N. Bevins, G. Chen, Interior tomography in X-ray differential phase contrast CT imaging, *Phys. Med. Biol.* 57 (2012) N117–N130.
- [42] A. Katsevich, Analysis of an exact inversion algorithm for spiral cone-beam CT, *Phys. Med. Biol.* 47 (2003) 2583–2597.



Renzhen Ye is currently an Associate Professor with the Department of Mathematics, Huazhong Agricultural University. Her research interests include partial differential equations, mathematical mechanization and mathematical physics, machine learning.



Yi Tang is currently with Department of Mathematics and Computer Science, Yunnan University of Nationalities, Kunming, China. His research interests include machine learning, statistical learning theory and pattern recognition.



Xiaoqiang Lu is currently an Associate Professor with the Center for OPTical IMagery Analysis and Learning (OPTIMAL), State Key Laboratory of Transient Optics and Photonics, Xian Institute of Optics and Precision Mechanics, Chinese Academy of Sciences, Xian, China. His current research interests include pattern recognition, machine learning, hyperspectral image analysis, cellular automata, and medical imaging.